Available online at www.sciencedirect.com
ScienceDirect
Journal of the Mechanics and Physics of Solids
55 (2007) 562–588

JOURNAL OF THE MECHANICS AND PHYSICS OF SOLIDS

www.elsevier.com/locate/jmps

The damage tolerance of elastic–brittle, two-dimensional isotropic lattices

Norman A. Fleck*, XinMing Qiu

Cambridge University Engineering Department, Trumpington Street, Cambridge CB2 1PZ, UK

Received 24 April 2006; received in revised form 18 August 2006; accepted 24 August 2006

Abstract

The fracture toughness of elastic–brittle 2D lattices is determined by the finite element method for three isotropic periodic topologies: the regular hexagonal honeycomb, the Kagome lattice and the regular triangular honeycomb. The dependence of mode I and mode II fracture toughness upon relative density is determined for each lattice, and the fracture envelope is obtained in combined mode I–mode II stress intensity factor space. Analytical estimates are also made for the dependence of mode I and mode II toughness upon relative density. The high nodal connectivity of the triangular grid ensures that it deforms predominantly by stretching of the constituent bars, while the hexagonal honeycomb deforms by bar bending. The Kagome microstructure deforms by bar stretching remote from the crack tip, and by a combination of bar bending and bar stretching within a characteristic elastic deformation zone near the crack tip. This elastic zone reduces the stress concentration at the crack tip in the Kagome lattice and leads to an elevated macroscopic toughness.

Predictions are given for the tensile and shear strengths of a centre-cracked panel with microstructure given explicitly by each of the three topologies. The hexagonal and triangular honeycombs are flaw-sensitive, with a strength adequately predicted by linear elastic fracture mechanics (LEFM) for cracks spanning more than a few cells. In contrast, the Kagome microstructure is damage tolerant, and for cracks shorter than a transition length its tensile strength and shear strength are independent of crack length but are somewhat below the unnotched strength. At crack lengths exceeding the transition value, the strength decreases with increasing crack length in accordance with the LEFM estimate. This transition crack length scales with the parameter of bar length divided by relative density of the Kagome grid, and can be an order of magnitude greater than the cell size at low relative densities. Finally, the presence of a boundary layer is noted at the free edge of a crack-free Kagome grid loaded in tension and in shear. Deformation within this boundary layer is by a combination of bar bending and stretching whereas remote from the free edge the Kagome

*Corresponding author.
E-mail address: naf1@eng.cam.ac.uk (N.A. Fleck).

0022-5096/$ - see front matter
doi:10.1016/j.jmps.2006.08.004

grid deforms by bar stretching (with a negligible contribution from bar bending). The edge boundary layer degrades both the macroscopic stiffness and strength of the Kagome plate. No such boundary layer is evident for the hexagonal and triangular honeycombs.

Keywords: Lattice materials; Fracture mechanics; Boundary layer; Honeycombs; Fracture

1. Introduction

There is much current interest in the development of 2D and 3D lattice materials comprising a periodic arrangement of rigid-jointed bars due to their favourable mechanical properties compared to stochastic foams (Deshpande et al., 2001a, b; Evans et al., 2000; Wadley et al., 2003). Three typical arrangements of 2D lattice materials possess an *isotropic* in-plane response: the regular hexagonal honeycomb, regular triangular honeycomb and the Kagome lattice, as sketched in Fig. 1. In each case, the lattice is made from bars of uniform thickness t and length ℓ. We shall study the fracture response of *elastic–brittle lattice materials* with these micro-architectures. They comprise rigidly jointed bars made from a linear elastic solid of Young's modulus E_s and fracture strength σ_f. The fracture toughness is determined for each microstructure by considering the asymptotic problem of a long crack in the lattice, with remote boundary loading defined by the K-field of linear elastic fracture mechanics. The regime of validity of linear elastic fracture is also explored by calculating the tensile and shear strengths of centre-cracked panels made from each lattice in turn.

The hexagonal and triangular lattices of Fig. 1 find practical application as ceramic catalytic converters for cars, and in heat exchangers and filters (Hunt, 1993; Gibson and Ashby, 1997). Thermal cracking is a serious technical problem, and expensive ceramic substrates of high thermal shock resistance are required. There is practical interest in determining whether the Kagome topology has a higher fracture toughness than the hexagonal and triangular lattices and thereby a greater damage tolerance to manufacturing and service flaws. We shall show that this is indeed the case. Additionally, the Kagome lattice in its two-dimensional (2D) and three-dimensional (3D) forms shows high potential for morphing applications (Hutchinson et al., 2003; Wicks and Guest, 2004; dos Santos e Lucato et al., 2004; Symons et al., 2005), yet its sensitivity to pre-existing flaws is unknown. For simplicity, we shall adopt a deterministic approach to predict the fracture toughness of the three lattices of Fig. 1, although it is recognised that the modulus of rupture σ_f of brittle cell walls has a statistical component. Variations in flaw size within the cell walls lead to variations in the modulus of rupture. Huang and Gibson (1991) have made use of Weibull statistics to include probabilistic effects in the fracture toughness of hexagonal and square honeycombs: typically, the statistical spread in strength is by a factor of 2–3. In contrast, we shall show in the present study that the fracture toughness can vary by several orders of magnitude with relative density, and with a change in geometry from one lattice to the next.

The macroscopic in-plane stiffness and strength of the hexagonal and triangular honeycombs and the Kagome lattice have been analysed recently, and they show a rich diversity in deformation response (Gibson and Ashby, 1997; Hutchinson et al., 2003; Wicks and Guest, 2004). The mode of deformation switches from bending-dominated for

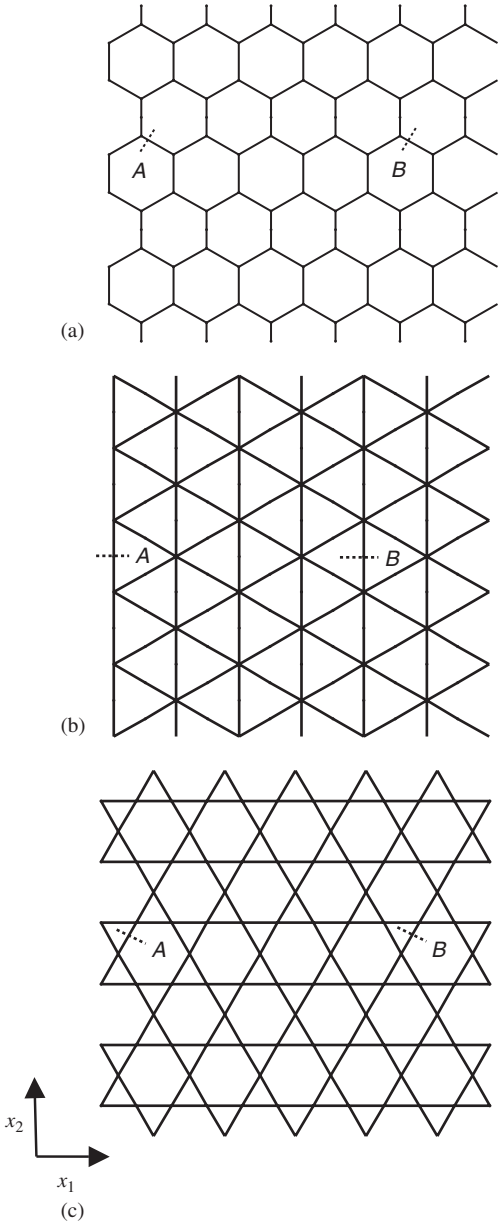

Fig. 1. The 2D lattices explored in this study: (a) hexagonal honeycomb, (b) triangular honeycomb and (c) Kagome lattice. The location A marks a site of maximum tensile stress in the surface cell, while the site B refers to a site of maximum local stress within the bulk of the Kagome lattice.

the hexagonal honeycomb, with a low connectivity of three bars meeting at each joint, to stretching dominated in the triangular honeycomb with a connectivity of six. The Kagome lattice is an intermediate case with a nodal connectivity of four: the infinite, perfect lattice deforms by bar-stretching under all uniform macroscopic stress-states, but missing bars or

misplaced nodes lead to a bending response near the imperfection, as discussed by Symons et al. (2005). A similar conclusion has also been reached by Wicks and Guest (2004): they considered the axial actuation of a single bar of the Kagome lattice, and calculated the elastic resistance of the remaining lattice to this bar extension. They showed that the Kagome lattice resists bar extension by a combination of axial stretching of some bars and bending of adjoining bars. The zone of deformation in the Kagome lattice resembles an elastic shear lag zone in a double lap shear specimen as used in adhesive testing. Wicks and Guest (2004) found that the length of the shear lag zone scales with the bar length ℓ divided by the relative density of the lattice, $\bar{\rho}$. Thus, the zone of deformation adjacent to the actuated bar increases from approximately 10 to 100ℓ when $\bar{\rho}$ is decreased from 10% to 1%. We shall show similar boundary layer effects for a cracked Kagome lattice: elastic boundary layers emanate from the crack tip, and these lead to remarkably high values of mode I and mode II fracture toughness. A boundary layer is also present at the free surface of an uncracked Kagome sheet and it is found that this leads to both a reduced stiffness and strength under either tensile or shear loading.

1.1. Scope of study

First, the in-plane stiffness and strength of elastic–brittle hexagonal and triangular honeycombs and the Kagome lattice are reviewed by making use of simple beam theory. Finite element calculations are performed to evaluate the crack tip elastic fields for each topology under combined mode I and mode II loadings. Upon assuming that the macroscopic fracture toughness is set by local tensile failure of any bar, scaling laws are determined for the dependence of mode I and mode II fracture toughnesses upon relative density. The role of the T-stress parallel to the crack in influencing the mode I fracture toughness is also addressed. The tensile and shear fracture strengths of a centre-cracked panel made from the three types of lattice are calculated directly, and the dependence of fracture strength upon crack length is compared with the predictions using linear elastic fracture mechanics (LEFM). Finally, a search is made for boundary layers at the lateral surface of the Kagome, triangular and hexagonal lattices subjected to either tensile or shear loading.

2. Review of the in-plane properties of isotropic lattice materials

2.1. Relative density

We begin by reviewing briefly the macroscopic stiffness and strength of these lattices by employing the analysis of Gibson and Ashby (1997). The relative density $\bar{\rho}$, as defined by the ratio of the density of the lattice material to the density of the solid, scales with the stockiness t/ℓ of each bar according to

$$\bar{\rho} = A\,\frac{t}{\ell}, \tag{1}$$

where the coefficient A depends upon architecture of lattice, as listed in Table 1. The linear relation (1) is adequate at low relative densities, but a quadratic term in t/ℓ is needed to correct for double-counting of the volume of material contained at the nodes.

Table 1
Coefficients for the scaling laws (1)–(3)

Topology	A	B	b	v	C	c
Hexagonal	$2/\sqrt{3}$	3/2	3	1	1/3	2
Triangular	$2\sqrt{3}$	1/3	1	1/3	1/3	1
Kagome	$\sqrt{3}$	1/3	1	1/3	1/2	1

2.2. Stiffness and strength

Simple beam theory can be used to determine the dependence of macroscopic Young's modulus E and macroscopic Poisson ratio v upon relative density $\bar{\rho}$ for the three lattices shown in Fig. 1. The scaling law can be adequately represented by the power-law expression

$$\frac{E}{E_s} = B\bar{\rho}^b, \tag{2}$$

where the values of the coefficient B and exponent b are listed in Table 1. The Poisson ratio v is independent of relative density, assuming $\bar{\rho}$ is sufficiently low for classical Euler–Bernoulli beam theory to apply, and its value is included in the table for each topology.

Beam theory can also be used to determine the macroscopic fracture strength of the elastic–brittle lattice, in the absence of macroscopic heterogeneities such as a macroscopic crack. Consider the lattices of Fig. 1 loaded macroscopically by in-plane, uniaxial tension. Each lattice responds in a linear-elastic manner, with a stress state within each bar given by simple beam theory. Failure initiates when the maximum local tensile stress within the lattice attains the tensile fracture strength of the solid σ_f. The corresponding macroscopic stress defines the fracture strength of the lattice. None of the three lattices of Fig. 1 possesses an isotropic fracture strength: the macroscopic tensile strength of the lattice varies with the orientation of the lattice. However, Gibson and Ashby (1997) have shown that the degree of anisotropy is small. For definiteness, we review here the macroscopic uniaxial strength σ_{c2} of the lattice, upon loading along the x_2 direction as shown in Fig. 1. The strength σ_{c2} can be expressed in terms of the tensile fracture strength of the solid, as

$$\frac{\sigma_{c2}}{\sigma_f} = C\bar{\rho}^c \tag{3}$$

with the coefficients (C, c) dependent upon geometry as stated in Table 1. The triangular and Kagome structures deform by bar stretching, and this leads to $b = c = 1$, while the hexagonal honeycomb deforms by bar bending, giving $b = 3$ and $c = 2$.

2.3. Fracture toughness

Less is known about the fracture toughness of lattice materials than their tensile properties: the authors have not been able to determine from the existing literature predictions for the macroscopic fracture toughness of the triangular honeycomb and the Kagome lattice. Maiti et al. (1984) and Gibson and Ashby (1997) argued that the mode I fracture toughness K_{IC} of an elastic–brittle hexagonal honeycomb is dictated by the

bending fracture of the cell wall immediately ahead of the crack tip. Upon assuming that brittle fracture occurs when the maximum local tensile stress anywhere in the lattice attains the tensile strength of the cell wall material σ_f, they determined that K_{IC} scales as

$$K_{IC} = 0.40\bar{\rho}^2\sigma_f\sqrt{\ell}. \tag{4}$$

The same problem has been addressed more recently by Chen et al. (1998). They replaced the hexagonal honeycomb by an effective Cosserat medium and calculated the asymptotic crack tip field, and thereby obtained

$$K_{IC} = 1.56\bar{\rho}\sigma_f\sqrt{\ell}. \tag{5}$$

This result gives a much higher toughness than Eq. (4) due to the linear rather than quadratic dependence upon $\bar{\rho}$. The experimental data quoted by Gibson and Ashby (1997) support the quadratic dependence of K_{IC} upon $\bar{\rho}$, and is taken here to be the correct result. The discrepancy can be traced to the fact that Chen et al. (1998) assumed affine deformation in their calculation of the effective properties of the Cosserat medium: this gives too stiff a response as it neglects the dominant contribution from cell wall bending under uniform loading. The analysis of Maiti et al. (1984) and Gibson and Ashby (1997) correctly includes the effect of cell wall bending and thereby gives the correct functional dependence of fracture toughness upon $\bar{\rho}$. In the present study we shall perform finite element calculations of the explicit microstructures to explore the crack tip field without the approximations inherent in the previous analytical studies of Maiti et al. (1984), Gibson and Ashby (1997) and Chen et al. (1998). Formula (4) is thereby validated, albeit with a slightly modified value of coefficient.

3. Finite element predictions of the fracture toughness of lattice materials

The crack tip field for the three topologies of Fig. 1 can be calculated by considering the asymptotic problem of a lattice containing a long crack in the (x_1, x_2) plane and its outer boundary subjected to the displacement field associated with the macroscopic crack tip K-field for a homogeneous and isotropic solid. Assume the crack is aligned along the negative x_1-axis, and enforce plane strain deformations such that the strain components vanish along the prismatic x_3-direction, see Fig. 2. Each of the lattices is transversely isotropic within the (x_1, x_2) plane. The modulus along the prismatic direction is $E_3 = \bar{\rho}E_S$, and the longitudinal Poisson ratios $\nu_{31} = \nu_{32}$ equal that of the solid, ν_S.

In order to apply the K-displacement field on the outer boundary of the mesh, it is necessary to make use of the effective elastic properties of each lattice. Assume plane strain conditions, such that $\varepsilon_3 = 0$ and thereby $\sigma_3 = \nu_{31}\sigma_1 + \nu_{32}\sigma_2$. Each lattice is transversely isotropic, and so the in-plane shear strain is related to the shear stress via the macroscopic shear modulus G,

$$\varepsilon_{12} = \frac{1}{2G}\sigma_{12}, \quad G \equiv \frac{E}{2(1+\nu)} \tag{6}$$

with G expressible in terms of the effective in-plane properties (E, ν) listed in Table 1. Enforcement of plane strain conditions along the prismatic x_3-direction modifies the in-plane response of the triangular honeycomb and Kagome lattice to the form

$$E_{ps}\varepsilon_1 = (\sigma_1 - \nu_{ps}\sigma_2) \quad \text{and} \quad E_{ps}\varepsilon_2 = (\sigma_2 - \nu_{ps}\sigma_1), \tag{7a}$$

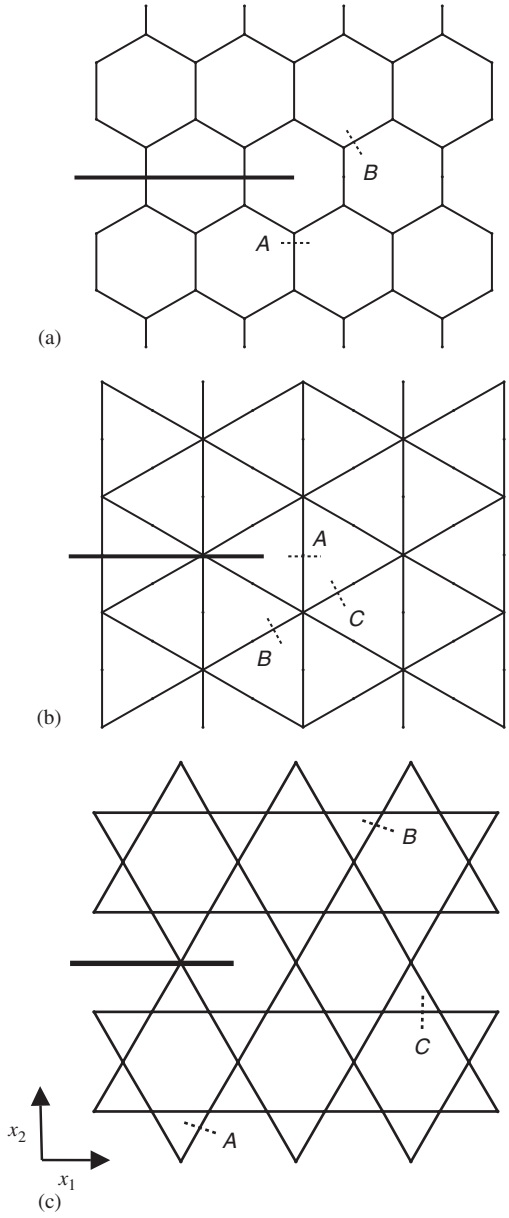

Fig. 2. A macroscopic, traction-free crack in relation to the lattice microstructure: (a) hexagonal, (b) triangular and (c) Kagome. The labels A, B and C in each sketch denote the predicted site of failure under combined mode I and mode II K-loading.

where

$$E_{\rm ps} = \frac{E}{(1-(1/3)\nu_{\rm s}^2)} \quad \text{and} \quad \nu_{\rm ps} = \frac{1+\nu_{\rm s}^2}{3-\nu_{\rm s}^2}. \tag{7b}$$

For the hexagonal honeycomb the plane strain modulus and Poisson ratio read

$$E_{\rm ps} = \frac{E}{(1-(3/2)\bar{\rho}^2 v_{\rm s}^2)} \quad \text{and} \quad \nu_{\rm ps} = \frac{2+3\bar{\rho}^2 v_{\rm s}^2}{2-3\bar{\rho}^2 v_{\rm s}^2}, \tag{8}$$

respectively. We note in passing that these relations for the hexagonal honeycomb are almost the same as those for plane stress, as the correction factor scales as $\bar{\rho}^2$.

The asymptotic crack tip field for a plane strain crack in an elastic solid is well-known, see for example Williams (1957) and standard texts such as Kanninen and Poplar (1985). For a crack along the negative x_1-axis, the displacement components (u_1, u_2) aligned with the Cartesian axes (x_1, x_2) can be expressed in terms of the polar co-ordinates (r, θ) centred on the crack tip as

$$u_1 = \frac{1}{2\sqrt{2\pi}} \frac{K_{\rm I}}{G} r^{1/2}(\kappa - \cos\,\theta)\cos\frac{\theta}{2} + \frac{1}{2\sqrt{2\pi}} \frac{K_{\rm II}}{G} r^{1/2}(\kappa + 2 + \cos\,\theta)\sin\frac{\theta}{2}, \tag{9a}$$

$$u_2 = \frac{1}{2\sqrt{2\pi}} \frac{K_{\rm I}}{G} r^{1/2}(\kappa - \cos\,\theta)\sin\frac{\theta}{2} - \frac{1}{2\sqrt{2\pi}} \frac{K_{\rm II}}{G} r^{1/2}(\kappa - 2 + \cos\,\theta)\cos\frac{\theta}{2}, \tag{9b}$$

where $K_{\rm I}$ and $K_{\rm II}$ are the mode I and mode II stress intensities, respectively, and $\kappa \equiv (3-\nu_{\rm ps})/(1+\nu_{\rm ps})$. The in-plane rotation field follows immediately as

$$\omega \equiv \frac{1}{2}(u_{2,1} - u_{1,2}) = -\frac{1+\kappa}{4\sqrt{2\pi}} \frac{1}{G} r^{-1/2}\left(K_{\rm I}\,\sin\frac{\theta}{2} + K_{\rm II}\,\cos\frac{\theta}{2}\right). \tag{9c}$$

The asymptotic crack tip field (9) is applied to the periphery of the finite element mesh for each lattice in turn. The details are as follows.

3.1. Finite element analysis

A square finite element mesh of each lattice has been created using ABAQUS (version 6.3), with crack tip region sketched in Fig. 2. Each lattice comprises about 100 unit cells by 100 unit cells, with a traction-free crack along the negative x_1-axis. For the case of triangular and Kagome lattices the joints along the negative x_1-axis are split on the $x_2 = 0$ plane, so that the lattice bars remain interconnected on each side of the crack, but have no connection across the cracking plane. The joints on the periphery of the finite element mesh are subjected to the asymptotic K-field (9).

Each bar of the lattice behaves as a plate, with plane strain conditions enforced along the x_3-axis. To achieve this, each bar is represented by a single *beam*-type finite element with Young's $E_{\rm s}'$ and Poisson ratio $\nu_{\rm s}'$ defined by

$$E_{\rm s}' = \frac{E_{\rm s}}{1-\nu_{\rm s}^2} \quad \text{and} \quad \nu_{\rm s}' = \frac{\nu_{\rm s}}{1-\nu_{\rm s}}. \tag{10}$$

This representation of a plate in plane strain by a beam is exact within the context of classical plate theory.

A quasi-static finite element analysis has been performed using Euler–Bernoulli beam elements with cubic interpolation functions (element type $B23$ in ABAQUS notation). It is assumed that the beams are each of thickness t and length ℓ, and are made from an elastic solid of modulus $E_{\rm s}'$ and Poisson ratio $\nu_{\rm s}'$. These elements capture the deflection of a slender beam with arbitrary end moments and shear forces, thus it suffices to represent each bar of

the lattice material by a single finite element; numerical checks confirmed the veracity of this result. All numerical simulations were performed using linear theory within the context of small strains and rotations.

3.2. Numerical predictions of mode I and mode II fracture toughness

The stress state in the vicinity of the crack tip has been calculated for pure mode I and pure mode II loadings, and for combined mode I–II loading. It is assumed that crack growth initiates when the maximum local tensile stress at the outermost fibre of any beam of the lattice attains the tensile fracture stress σ_f of the solid. The predicted mode I fracture toughness K_{IC} and mode II fracture toughness K_{IIC} are plotted as a function of relative density $\bar{\rho}$ in Fig. 3, for the choice $v_s = 1/3$. Numerical experimentation confirmed that the lattice grid is sufficiently large for the solution to have converged.

The finite element results confirm that the mode I and mode II fracture toughnesses scale with $\bar{\rho}$ according to the power law,

$$\frac{K_C}{\sigma_f\sqrt{\ell}} = D\bar{\rho}^d. \tag{11}$$

It is evident from Fig. 3 that the exponent d equals 2 for the hexagonal honeycomb, equals unity for the triangular honeycomb and equals $\frac{1}{2}$ for the Kagome lattice. For each topology, the pre-exponent D is slightly less for mode II loading than for mode I loading, see Table 2. It is remarkable that the Kagome lattice has a very low sensitivity of fracture toughness to relative density, as evidenced by the curve-fitted value of $d = \frac{1}{2}$.

An additional set of calculations has been performed in order to explore the sensitivity of fracture toughness of the Kagome lattice to the orientation of the macroscopic crack. The cracking plane was rotated by 30° relative to the microstructure and the toughness was calculated for $\bar{\rho}$ in the range 0.003–0.2. At any given relative density it is found that rotation of the crack by 30° leads to a drop by 10% in the predicted value of K_{IC} but to a negligible change in the magnitude of K_{IIC}.

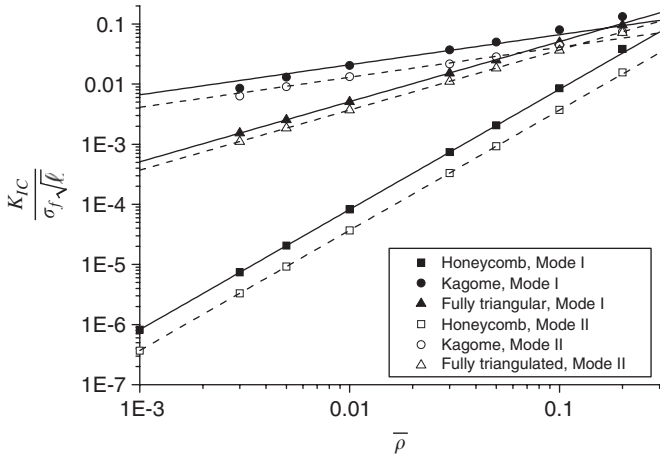

Fig. 3. The predicted mode I fracture toughness K_{IC} and mode II fracture toughness K_{IIC} plotted as a function of relative density $\bar{\rho}$, for the three lattices.

Table 2
Value of the pre-exponent D for mode I and mode II loadings, for the scaling law (11)

Topology	D for mode I	D for mode II	d for both modes
Hexagonal	0.800	0.370	2
Triangular	0.500	0.380	1
Kagome	0.212	0.133	0.5

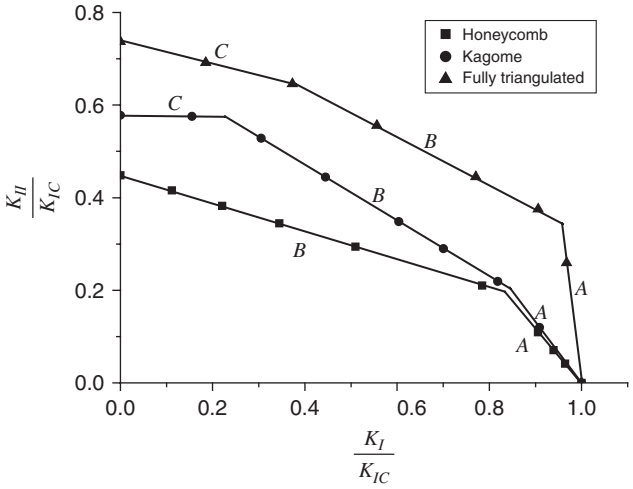

Fig. 4. The failure envelope for mixed mode loading. The segments of the failure surface correspond to the critical sites of failure shown in Fig. 2.

3.3. Prediction of the fracture toughness under mixed mode loading

The fracture locus in (K_I, K_{II}) space has been explored for each of the three lattices. The results are shown in Fig. 4 for the choice $\bar{\rho} = 5\%$, and for each lattice the values (K_I, K_{II}) have been normalised by the mode I fracture toughness K_{IC}. Sample numerical experiments confirmed that the normalised failure locus is insensitive to the value of $\bar{\rho}$ over the range of interest, $0.001 < \bar{\rho} < 0.2$. For each topology, the locus comprises the inner convex envelope of a series of straight lines, corresponding to a particular failure site. The straight segments of the failure locus are marked as A, B and C in Fig. 4 and the corresponding failure locations are given in Fig. 2. We conclude from Fig. 4 that the triangular lattice is the most resistant to mode II loading, and the failure envelope is approximately circular in shape. In contrast, the failure envelope for the honeycomb lattice is the most eccentric in shape, with a relatively low value of mode II toughness.

Recall that each bar of the lattice materials is represented by Euler–Bernoulli beam theory. The longitudinal stress varies linearly across the section of each beam and comprises the sum of an axial stress

$$\sigma_a = \frac{F}{t} \tag{12a}$$

and a bending stress of amplitude

$$\sigma_b = \frac{6M}{t^2}, \tag{12b}$$

where F and M are, respectively, the axial force and bending moment per unit thickness in the out-of-plane x_3 direction. An examination of the stress state within each cracked lattice reveals that the hexagonal honeycomb fails by the bending of its bars, with the magnitude of axial stress σ_a only a few percent that of the bending stress σ_b at the failure site, for both mode I and mode II loadings. Failure initiates in the hexagonal cells adjacent to the crack tip cell, and the failure location is included in Fig. 2: the location switches from site A under mode I loading to site B under mode II loading. Second, consider the triangular honeycomb. The stress state involves predominantly stretching of the bars, and the bending stress is only a few percent of the axial stress at the failure site. As the mode mix ranges from mode I to mode II, the failure location switches from site A (the bar directly ahead of the crack tip) to site B (below the crack tip) and then to site C (off the cracking plane and somewhat ahead of the crack tip), see Fig. 2. And third, consider the Kagome lattice. The failure site is located at a distance of several ℓ from the crack tip, and shows the reverse trend to that of the fully triangular honeycomb: as the mode mix switches from mode I to mode II, the site switches from site A above the crack tip (and its mirror-image below the cracking plane) to site B (off the crack plane and ahead of the crack tip) and thence to site C ahead of the crack tip. For both mode I and mode II loadings, an examination of the relative proportion of bending to stretching stress of the critical bar in the Kagome lattice reveals that the amplitude of the bending stress is comparable to that of the axial stress. For example, at $\bar{\rho} = 5\%$ the ratio σ_a/σ_b equals 0.79 for mode I loading and equals 0.46 for mode II loading.

3.4. Discussion of toughness predictions

The relative magnitudes of bending stress to axial stress are consistent with the arguments of Deshpande et al. (2001a) and of Wicks and Guest (2004). A connectivity value of 3 bars per node for the hexagonal honeycomb is sufficiently low for it to deform in a bending mode, while the high connectivity value of 6 for the triangular honeycomb causes it to deform by cell wall stretching. The Kagome lattice has the transition value of connectivity equal to 4. Under uniform loading this lattice deforms by bar stretching, but upon introduction of defect such as a macroscopic crack the bars deform by a combination of bar stretching and bar bending. Wicks and Guest (2004) introduced an alternative defect in the Kagome lattice. They calculated the resistance of the lattice to axial extension of a single bar and found that the surrounding Kagome lattice responds by a combination of bar stretching and bar bending, with the amplitude of the bending stress comparable to the level of axial stress in the most highly stressed bars.

The analysis of Chen et al. (1998) gives similar results to those reported here in Table 2 for the triangular honeycomb: they find ($d = 1$, $D = 1.33$) for mode I and ($d = 1$, $D = 0.433$) for mode II loading. In contrast, for the hexagonal honeycomb, the current prediction of $d = 2$ is in line with the theoretical treatment of Maiti et al. (1984) and Gibson and Ashby (1997), but deviates from the prediction of Chen et al. (1998) who deduced that $d = 1$. As discussed above, the analysis of Chen et al. (1998) is based upon an overly stiff constitutive model for the honeycomb. The coefficient D in Eq. (11) for the

hexagonal honeycomb under mode I loading has the best-fitting value of 0.80, as given by Table 2. This corrects the value of $D = 0.40$ in Eq. (4), as derived by Gibson and Ashby (1997) by an approximate analytical argument.

The mode I crack tip opening profile is plotted in Fig. 5a for the hexagonal honeycomb, and in Fig. 5b for the triangular honeycomb and Kagome lattice. The crack profile is also evident from the deformed mesh displayed in Fig. 6 for each lattice, for the choice $\bar{\rho} = 5\%$. All the crack opening profiles collapse onto a single curve of $E\delta_I/K_I\sqrt{\ell}$ versus $|x_1|/\ell$ for the triangular honeycomb, see Fig. 5b, and nearly do so for the hexagonal honeycomb, see Fig. 5a. For the hexagonal and triangular honeycombs, the crack opening displacement δ_I depends upon the distance $|x_1|$ behind the crack tip according to the familiar relation of LEFM

$$\frac{E\delta_I}{K_I\sqrt{\ell}} \propto \sqrt{\frac{|x_1|}{\ell}}, \tag{13}$$

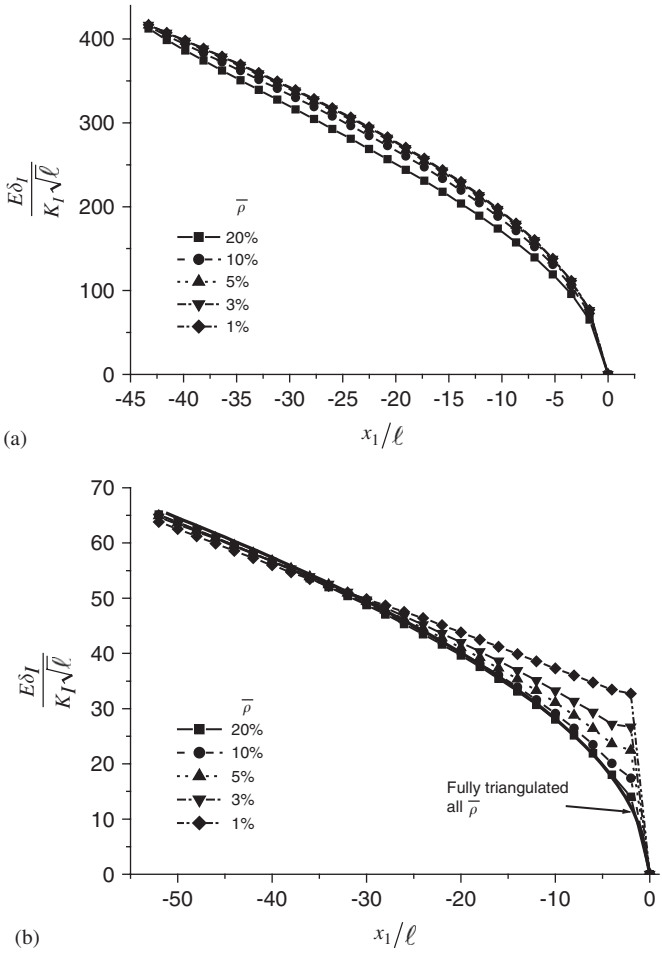

Fig. 5. Mode I crack opening displacement field for (a) hexagonal honeycomb and (b) triangular honeycomb and Kagome lattice.

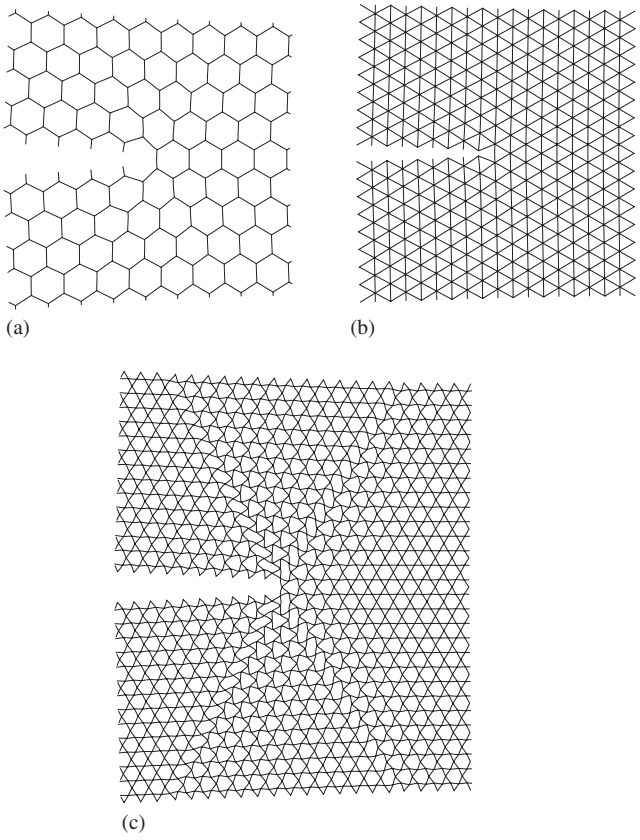

Fig. 6. Deformed mesh under mode I loading for (a) hexagonal honeycomb, (b) triangular honeycomb and (c) Kagome lattice. The relative density is $\bar{\rho} = 5\%$.

where the effective modulus E of each lattice depends upon the relative density $\bar{\rho}$ according to Eq. (2). The Kagome lattice behaves differently. Whilst the usual K-field is preserved remote from the crack tip it is violated near the crack tip due to an *elastic blunting phenomenon*. A regression analysis has been performed on the crack tip opening of the Kagome lattice one joint back from the crack tip. It is found that the crack tip opening $\delta_{\mathrm{I}}^{\mathrm{tip}}$ scales with $\bar{\rho}$ according to

$$\frac{E\delta_{\mathrm{I}}^{\mathrm{tip}}}{K_{\mathrm{I}}\sqrt{\ell}} = \frac{8.2}{\bar{\rho}^{1/3}}. \tag{14}$$

Now consider the deformed mesh for each lattice under mode II loading. The crack profile is evident from the deformed mesh displayed in Fig. 7 for the choice $\bar{\rho} = 5\%$. Again, elastic blunting is evident for the Kagome lattice but not for the other two lattices. Additional finite element simulations (not shown) reveal that the functional form of Eq. (13) is observed for mode II loading of the hexagonal and triangular honeycombs.

The normal and shear traction on the plane immediately ahead of the crack tip has also been explored by the finite element calculations. Recall that the continuum solution suggests that the traction ahead of the crack tip varies with distance x_1 ahead of the crack

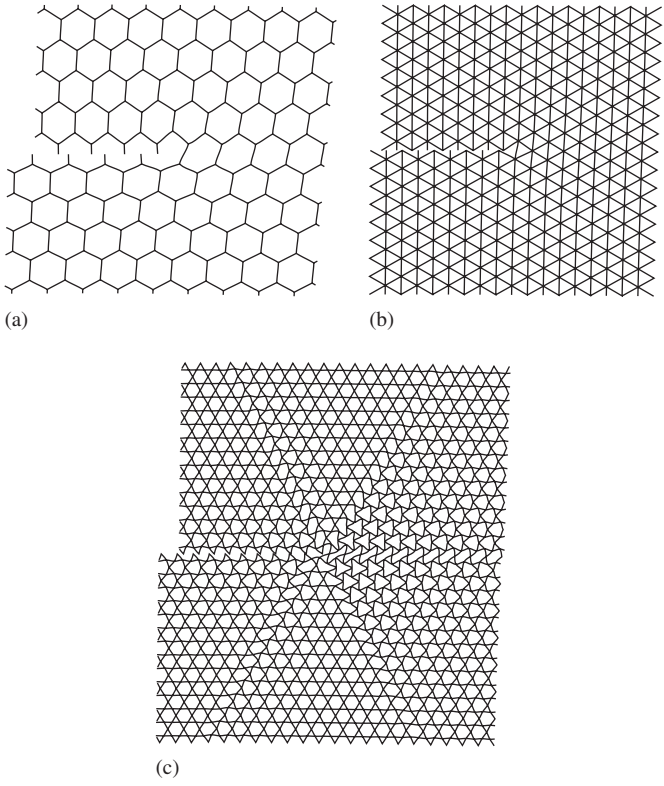

Fig. 7. Deformed mesh under mode II loading for (a) hexagonal honeycomb, (b) triangular honeycomb and (c) Kagome lattice. The relative density is $\bar{\rho} = 5\%$.

tip according to $1/\sqrt{x_1}$. Similarly, for the hexagonal and triangular honeycomb under both mode I and mode II loadings it is found that the axial load on each bar ahead of the crack tip varies as $1/\sqrt{x_1}$. In contrast, for the Kagome lattice under mode I or mode II loading, the traction is almost independent of distance from the crack tip over a distance of several cell sizes ahead of the crack tip; the domain of almost uniform traction extends about 4ℓ ahead of the crack tip at $\bar{\rho} = 5\%$, and this zone increases to about 20ℓ at $\bar{\rho} = 1\%$. Explicit plots are omitted for the sake of brevity.

Additional insight into the deformation responses of the lattices is gained by inspecting the deformed meshes under mode I and mode II loadings, see Figs. 6 and 7, respectively, for the choice $\bar{\rho} = 5\%$. Local to the crack tip, the hexagonal honeycomb deforms by bar bending, the triangular lattice stretches while the Kagome lattice has an elastic deformation zone near the crack tip involving both bar bending and stretching. Remote from the crack tip, the Kagome lattices stretches. It is evident from Fig. 6 that the deformation zone in mode I extends furthest from the crack tip along a radial line inclined at about 60° to the cracking plane, while from Fig. 7 the deformation zone extends directly ahead of the crack tip in mode II. Numerical experimentation reveals that the size of the characteristic crack tip elastic zone of the Kagome lattice increases with decreasing relative density for both mode I and mode II loadings. In order to make this precise, a criterion is

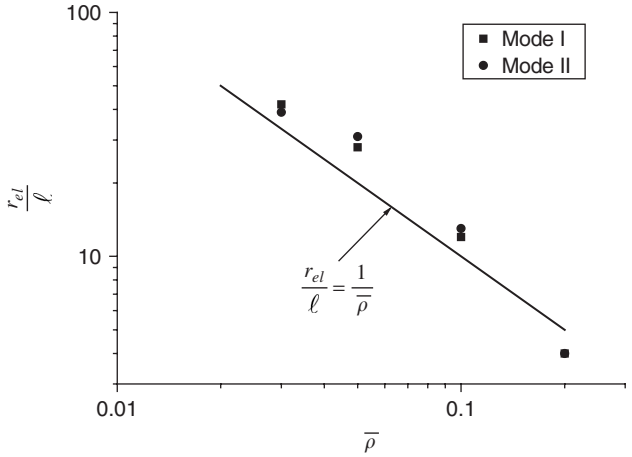

Fig. 8. The length of the elastic shear zone extending from the crack tip in the Kagome lattice.

needed for the size of the crack tip deformation zone. An arbitrary choice for the extent of the crack tip deformation zone is the radial distance $r_{\rm el}$ from the crack tip over which the magnitude of joint rotation $|\omega|$ exceeds $K/E\sqrt{\ell}$. The dependence of $r_{\rm el}$ upon $\bar{\rho}$ is shown in Fig. 8 for both mode I and mode II loadings. The calculations support the simple scaling law,

$$\frac{r_{\rm el}}{\ell} = \frac{4.5}{\bar{\rho}} \tag{15}$$

for both modes I and II.

4. Analytical prediction of the fracture toughness of lattice materials

4.1. Hexagonal honeycomb

It has already been noted above that Maiti et al. (1984) and Gibson and Ashby (1997) have made an analytical estimate for the fracture toughness of elastic–brittle hexagonal honeycombs. They assume that the crack tip K-field of a continuum is maintained to the crack tip of a honeycomb, and they take the crack tip to be positioned at the centre of one cell. The cell wall immediately ahead of the crack tip fails in bending due to the applied normal traction on the cracking plane from the K-field. The fracture toughness K_{IC} scales with the tensile strength of the cell wall material $\sigma_{\rm f}$ according to Eq. (4). A closely related argument is now used to estimate the mode II fracture toughness for the hexagonal honeycomb. The shear traction immediately ahead of the crack tip is used to estimate the bending moment on the cell walls of the crack tip cell. In brief, when a shear traction τ^∞ is applied to a hexagonal honeycomb, the maximum bending stress $\sigma_{\max}$ induced in the cell walls is $\sigma_{\max} = 4\sqrt{3}\tau^\infty/\bar{\rho}^2$, as discussed in Section 4.3 of Gibson and Ashby (1997). Recall that the shear traction in a homogeneous elastic solid, a distance r immediately ahead of a crack tip in mode II is $\tau^\infty = K_{\rm II}/\sqrt{2\pi r}$. Assume that this formula is preserved for the traction ahead of the crack tip in a hexagonal honeycomb, and place the crack tip at the

centre of a hexagonal cell, such that $r = \sqrt{3}\ell$. Then, the predicted mode II toughness K_{IIC} follows as

$$K_{IIC} = 0.48\bar{\rho}^2\sigma_f\sqrt{\ell}. \tag{16}$$

As expected, this relation is of the same functional form as Eq. (4), with a minor change to the numerical coefficient.

4.2. Triangular honeycomb

The mode I and mode II fracture toughnesses of the triangular honeycomb can be calculated in a similar manner to those described above for the hexagonal honeycomb. Consider first the mode I problem, with the crack aligned with the negative x_1 axis. Recall that the stress field immediately ahead of a mode I crack in a continuum is related to the applied mode I stress intensity factor K_I by

$$\sigma_{11} = \sigma_{22} = \frac{K_I}{\sqrt{2\pi x_1}} \quad \text{and} \quad \sigma_{12} = 0. \tag{17}$$

The average value of these stresses over one cell dimension ahead of the crack tip is

$$\bar{\sigma}_{11} = \bar{\sigma}_{22} = \frac{2}{\ell\sqrt{3}}\int_0^{(\ell\sqrt{3})/2}\left[\frac{K_I}{\sqrt{2\pi r}}\right]\mathrm{d}r = \frac{3^{1/4}4}{\sqrt{12\pi}}\frac{K_I}{\sqrt{\ell}} \quad \text{and} \quad \bar{\sigma}_{12} = 0. \tag{18}$$

Now assume that this average stress state is in equilibrium with the stresses within each bar. Label bars inclined at 30° to the x_1-axis as bars of type a, bars aligned with the x_2-axis as bars of type b, and bars aligned at −30° to the x_1-axis as bars of type c. Then, equilibrium dictates that the axial stress (σ_a, σ_b, σ_c) in bars (a, b, c) are

$$\begin{pmatrix}\sigma_a\\ \sigma_b\\ \sigma_c\end{pmatrix} = \frac{1}{\bar{\rho}}\begin{pmatrix}\sqrt{3} & 0 & 2\sqrt{3}\\ -\sqrt{3} & 3 & 0\\ \sqrt{3} & 0 & -2\sqrt{3}\end{pmatrix}\begin{pmatrix}\bar{\sigma}_{11}\\ \bar{\sigma}_{22}\\ \bar{\sigma}_{12}\end{pmatrix}. \tag{19}$$

Substitution of Eq. (19) into Eq. (18) reveals that the largest axial stress is experienced by bars a and c, with

$$\sigma_a = \sigma_c = \frac{3^{1/4}4}{\sqrt{\pi}}\frac{K_I}{\bar{\rho}\sqrt{\ell}}. \tag{20}$$

Now assume that fracture initiates when the local axial stress attains the fracture strength σ_f. Then, the predicted mode I fracture toughness reads

$$K_{IC} = 0.337\bar{\rho}\sigma_f\sqrt{\ell}. \tag{21}$$

This analytical estimate is in reasonable agreement with the finite element predictions: recall from Table 2 that the numerical simulations suggest a linear dependence of K_{IC} upon $\bar{\rho}$, with the pre-exponent D equal to 0.5.

A parallel calculation can be performed for mode II loading, and the predicted mode II fracture toughness reads

$$K_{IIC} = 0.169\bar{\rho}\sigma_f\sqrt{\ell}. \tag{22}$$

This again compares favourably with the finite element predictions: the numerical simulations suggest a linear dependence of K_{IIC} upon $\bar{\rho}$, with the pre-exponent D equal to 0.38, as given in Table 2.

4.3. Kagome lattice

The Kagome lattice has an exceptionally high fracture toughness due to the presence of a crack tip blunting zone. A simple scaling argument is now used to estimate the macroscopic mode I fracture toughness. It has already been stated in (15) that an elastic blunting zone of length $r_{el} = 4\ell/\bar{\rho}$ emanates from the crack tip. The displacements at the outer edge of this zone match the K displacement field and thereby scale as $K\sqrt{r_{el}}/E$. It is clear from the deformed mesh of Fig. 6(c) that displacements of this magnitude persist down to the crack tip and give rise to crack tip blunting. We may estimate the level of bending stress in the crack tip bars as follows. Consider as a subsidiary problem, a built-in beam of length ℓ and thickness t, subjected to a transverse end deflection δ. The bending stress at the root of the beam is of magnitude $\sigma_b \approx E_s t\delta/\ell^2$. Now equate δ with $K\sqrt{r_{el}}/E$, and let σ_b equal the fracture strength σ_f. Then, the predicted fracture toughness is

$$K_{IC} \approx \bar{\rho}^{1/2}\sigma_f\sqrt{\ell}. \tag{23}$$

This expression gives the correct functional dependence of K_{IC} upon $\bar{\rho}$ to within an unknown numerical constant. The full finite element analysis supports (23) for both mode I and mode II loading, and reveals that the constant of proportionality equals 0.212 for mode I, and equals 0.133 for mode II, as listed in Table 2.

5. The role of the T-stress in the crack tip field

It is well-known that the second term in the series expansion of the mode I crack tip field is the so-called T-stress parallel to the crack plane. The T-stress scales linearly with the remote applied stress, but its magnitude depends upon the specimen configuration. The T-stress vanishes for mode II loading, by a symmetry argument. For conventional, fully dense, elastic–brittle solids the T-stress plays a relatively minor role in influencing the fracture processes at the crack tip. In ductile fracture and fatigue, however, the T-stress becomes important at short crack lengths and reveals itself in a dependence of inferred fracture toughness upon specimen geometry, see for example Fleck (1986). For example, for a centre-crack in an infinite sheet under remote tension σ_∞, the T-stress is given by $T = -\sigma_\infty$, while for an edge cracked sheet under remote tension $T \approx 0$, see for example Rice (1974) and Larsson and Carlsson (1973). In elastic–plastic solids tested in plane strain, the plastic zone size decreases with increasing positive T-stress; Shercliff and Fleck (1990) have shown experimentally and theoretically that this leads to a dependence upon specimen geometry of fatigue crack growth retardation following a single peak overload.

In the brittle fracture of lattice materials no experimental data exist on the relevance of the T-stress to the fracture strength of cracked finite geometries. Predictions are made in the following section for a centre cracked panel and it is shown that it is necessary to include T-stress effects to explain the predicted strengths at sufficiently low relative densities, particularly for the hexagonal honeycomb.

In this section, a T-stress is applied along the x_1 direction at the periphery of an edge-cracked square mesh of side length $2w$, with crack tip geometry as shown in Fig. 2.

The T-stress is applied by prescribing a normal traction T along the lateral sides of the mesh. The local stress in each of the three lattices is calculated as a function of relative density at the potential failure sites for remote mode I loading.

5.1. Finite element predictions of crack tip stresses associated with the T-stress

Consider first the stress state induced in the hexagonal honeycomb by application of the T-stress parallel to the cracking plane. Finite element simulations were performed for $\bar{\rho}$ in the range 0.003–0.3, and the local tensile stresses σ_A and σ_B at sites A and B of Fig. 2 were determined. These stresses are associated with bending of the struts and are adequately expressed by the regression fits

$$\sigma_A = 0 \quad \text{and} \quad \sigma_B = -2.9\,\frac{T}{\bar{\rho}^2}. \tag{24}$$

We shall show below in a case study on the centre-cracked panel subjected to uniaxial tension that the large negative T-stress is sufficient to switch the location of failure from location A to location B.

Second, consider the Kagome lattice and triangular honeycomb. For both geometries the local stress σ_A scales linearly with $T/\bar{\rho}$ and is given by

$$\sigma_A = -0.45\,\frac{T}{\bar{\rho}} \tag{25}$$

for the Kagome lattice and

$$\sigma_A = -0.65\,\frac{T}{\bar{\rho}} \tag{26}$$

for the triangular lattice. The significance of the T-stress in influencing the fracture strength of the centre-cracked panel is now explored.

6. Numerical prediction of fracture strength of centre-cracked panel made from lattice materials

The fracture toughness predictions made above by the finite element method allow for an estimation of the tensile fracture strength of lattice materials containing finite cracks. But what is the damage tolerance of a lattice material containing a crack which is comparable in length to the cell size ℓ? In order to address this, explicit finite element simulations have been performed on panels of width $2w$, containing a centre-crack of length $2a$. The panels are subjected to remote tension, equi-biaxial tension and to remote shear as shown in Fig. 9, and the magnitude of the remote stress required to initiate crack growth is determined as a function of crack length.

Finite element simulations have been formed using a square mesh of side length 200ℓ using the same elements as for the K-field problem: Euler–Bernoulli beam elements were used with cubic interpolation functions (element type $B23$ in ABAQUS notation). The local crack tip geometry is the same as that shown in Fig. 2. Write the applied stress level for tensile failure under uniaxial and equi-biaxial loading as σ_c, and write the critical value of applied shear stress as τ_c. Then, the critical values of σ_c/σ_f and τ_c/σ_f are plotted against crack length in Fig. 10(a) for the hexagonal honeycomb, in Fig. 10(b) for the triangular

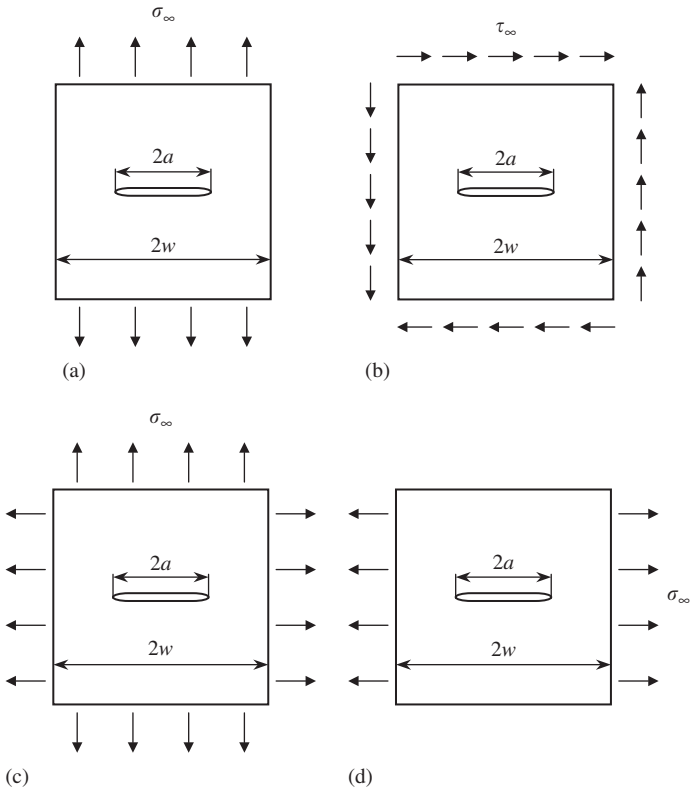

Fig. 9. The centre-cracked panel under (a) remote axial tension, (b) remote shear, (c) equi-biaxial tension and (d) transverse tension.

honeycomb and in Fig. 10(c) for the Kagome lattice. Results are illustrative with $\bar{\rho}$ taken as 5% for the hexagonal and triangular honeycombs while $\bar{\rho} = 10\%$ for the Kagome lattice; the higher value of relative density is used for the Kagome lattice in order to minimise the size and significance of a boundary layer which exists at the sides of the panel for this lattice. A full discussion on this boundary layer is given in a subsequent section. The main purpose of Fig. 10 is to assess the accuracy of predictions using LEFM rather than to compare the absolute value of fracture strength from one topology to the next. Thus, the two different choices in value for $\bar{\rho}$ is of minor concern. In plotting the results, the crack length $2a$ is taken to span the distance between intact cell walls, rather than taking the crack tips to be positioned at the centre of a cell as sketched in Fig. 2. Thus, for the hexagonal honeycomb, the crack semi-length for a single missing cell wall is taken as $a = \sqrt{3}\ell$. Similarly, for the triangular honeycomb and for the Kagome lattice, the semi-crack length for a single missing cell wall is $a = \sqrt{3}\ell/2$ and $a = 2\ell$, respectively. These limiting cases with a single missing cell wall are denoted by the left-most data points in Fig. 10.

Some broad conclusions can be drawn. The uniaxial tensile strength, biaxial strength and the shear strength drop with increasing crack length, with the biaxial strength consistently the highest and the shear strength the least at any given crack length. It is

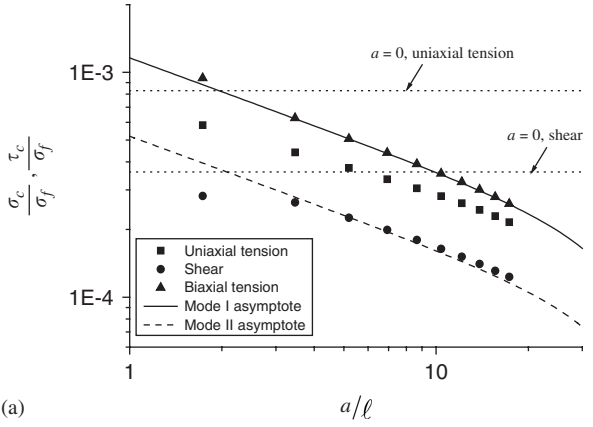

(a)

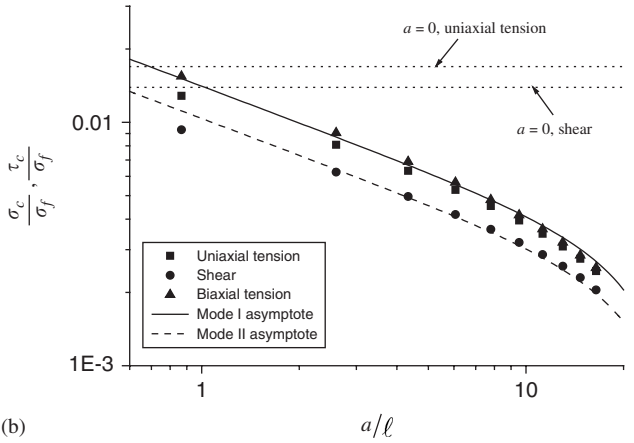

(b)

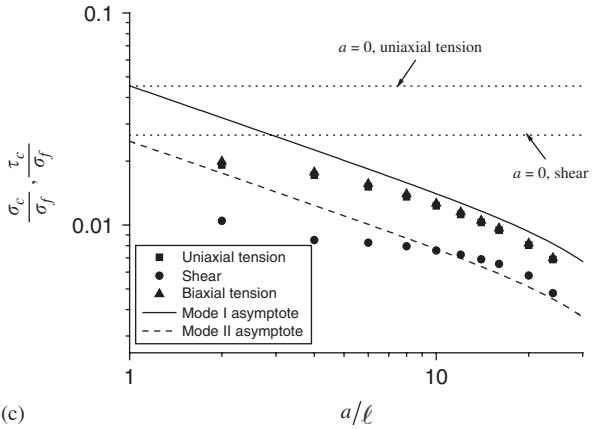

(c)

Fig. 10. The strength of a centre-cracked panel made from (a) hexagonal honeycomb ($\bar{\rho} = 5\%$), (b) triangular honeycomb ($\bar{\rho} = 5\%$) and (c) Kagome lattice ($\bar{\rho} = 10\%$).

instructive to compare the tensile strength and shear strength of the centre-cracked panels containing explicit microstructures with the continuum predictions (11).

6.1. Shear strength for each lattice

Consider first the shear strength for each of the three lattices. The mode II stress intensity factor K_{II} is related to the applied shear stress τ on the ends of the centre-cracked panel according to (Brown and Srawley, 1966),

$$K_{\mathrm{II}} = \tau\sqrt{\pi a}\sqrt{\sec\left(\frac{\pi}{2}\frac{a}{w}\right)}. \tag{27}$$

The corresponding shear strength τ_{c} is obtained by equating K_{II} to the $K_{\mathrm{II}C}$ values of Eq. (11) using the curve fitted values for (D, d) from Fig. 3. The shear strength based on $K_{\mathrm{II}C}$ is in good agreement with the shear strength for a finite crack in the three lattice materials, provided the crack length a exceeds 3ℓ for the hexagonal honeycomb, 10ℓ for the Kagome lattice and 1ℓ for the triangular honeycomb. At shorter crack lengths than these transition values, the shear strength for each lattice is approximately constant and is somewhat below the unnotched shear strength (shown by a dotted line, and labelled $a = 0$ in Fig. 10) due to a stress concentration associated with removal of one or more bars. Numerical experimentation reveals that this knock-down factor in shear strength is independent of relative density for each lattice.

6.2. Tensile strength for each lattice

The mode I stress intensity factor K_{I} is related to the applied tensile stress σ_2 on the ends of the centre-cracked panel according to Brown and Srawley (1966),

$$K_{\mathrm{I}} = \sigma_2\sqrt{\pi a}\sqrt{\sec\left(\frac{\pi}{2}\frac{a}{w}\right)}. \tag{28}$$

The predicted tensile strength σ_{c} is obtained by equating K_{I} to the $K_{\mathrm{I}C}$ values of Eq. (11) with the curve fitted values for (D, d) from Fig. 3. The predicted locus of σ_{c} is included in Figs. 10(a)–(c), and is in excellent agreement with the biaxial strength for the hexagonal and triangular honeycombs. This is consistent with the fact that the net T-stress in the centre-cracked panels under biaxial tension is close to zero. The biaxial strength for the Kagome lattice is about 10% less than that predicted from its $K_{\mathrm{I}C}$ value, see Fig. 10(c); this is explained by the fact that a large elastic shear zone is present at the crack tip and a boundary layer also exists at the sides of the panel width. A much larger mesh would be needed in order to obtain better agreement with the LEFM prediction. The presence of this free-surface boundary layer is discussed further in a subsequent section below. Now, consider the uniaxial tensile strength for the centre-cracked panel made from each lattice in turn.

(i) For the *hexagonal honeycomb*, the uniaxial strength is less than the biaxial strength by a factor of approximately 2. The location of the failure site in the lattice as defined in Fig. 2(a) also switches with the nature of the remote loading: the lattice fails at site B for uniaxial loading of the centre-cracked panel and at site A for biaxial loading. Recall that the failure site is at site A for a semi-infinite crack under mode I loading and in the

absence of the T-stress, as discussed in Section 3.3. The explanation for the reduced strength of the cracked panel under uniaxial loading lies in the fact that this geometry generates a large negative T-stress. The T-stress at the crack tip generates additional loading as quantified by Eq. (24), and this additional loading switches the failure site from A to B. Recall the T-stress for a centre-cracked panel is of magnitude $T \approx -1.1\sigma_2$, and so equibiaxial loading has the effect of almost eliminating the T-stress. Consequently, the tensile strength for equibiaxial loading is in excellent agreement with the tensile strength as predicted via the K_{IC} value for the lattice, using Eq. (28). We further note from Fig. 10(a) that the uniaxial tensile strength at short crack lengths, $a/\ell \approx 2$, is less than the unnotched tensile strength due to the introduction of a stress concentration factor associated with the removal of one horizontal bar.

(ii) For the *triangular honeycomb* and the *Kagome lattice*, the uniaxial strength is comparable to the biaxial strength, and the failure site remains invariant (site A of Fig. 2c). This insensitivity is due to the high toughness and the relatively low stresses (25 and 26) induced by the macroscopic T-stresses for these lattices.

6.3. Transition flaw size

We have already noted from Fig. 10 that the tensile strength of a centre-cracked panel switches from a value on the order of the uniaxial unnotched strength to the value given by LEFM with increasing crack length. A transition value of crack length can be identified as follows, for each morphology of lattice.

Consider a centre-cracked infinite panel made from a lattice material, containing a crack of length $2a$ and subjected to a remote tensile stress Σ_2. The material has a tensile strength given by Eq. (3) in the absence of the crack, whereas for long cracks the tensile strength is given by

$$\Sigma_2 = \frac{K_{IC}}{\sqrt{\pi a}} \tag{29}$$

with the mode I fracture toughness K_{IC} given in Eq. (11). By equating (3) and (20), a simple analytical estimate can be made for the transition crack length a_T at which the tensile strength switches from the value of Eq. (3) to the value given in Eq. (20). The result is

$$a_T = \frac{1}{\pi}\left(\frac{K_{IC}}{\sigma_{c2}}\right)^2 \tag{30}$$

and upon making use of Eqs. (3) and (11), this can be re-written as

$$\frac{a_T}{\ell} = \frac{1}{\pi}\left(\frac{D}{C}\right)^2 \bar{\rho}^{2(d-c)}. \tag{31}$$

Now make use of the coefficients listed in Tables 1 and 2 to obtain $a_T = 1.833\ell$ for the hexagonal honeycomb, $a_T = 0.716\ell$ for the triangular honeycomb and $a_T = 0.0572\ell/\bar{\rho}$ for the Kagome lattice. We conclude that the transition flaw size is independent of relative density and is of order ℓ for the hexagonal and triangular honeycombs. In contrast, the transition flaw size of the Kagome lattice scales with $1/\bar{\rho}$ and is several times ℓ at low relative densities. For example, at $\bar{\rho} = 1\%$, we have $a_T = 5.7\ell$ implying that the lattice has moderate damage tolerance: for centre-cracks of length less than 11.4ℓ the tensile strength scales with the

unnotched strength and not with the fracture toughness. The interested reader is referred to the overview by Fleck et al. (1994) for a full discussion of the significance of the value of a_T in engineering design for both monotonic and cyclic loading of engineering materials.

7. The effect of a free boundary upon the tensile strength of the three lattices

It is of practical significance to determine whether the free surface of a lattice material gives rise to a boundary layer in deformation under macroscopic loading, with associated stress concentrations. In general, the stress state of bars internal to the lattice materials is not sustainable at the free surface due to the reduced connectivity, and so by St. Venant's principle a boundary layer may be required in order to diffuse the load distribution from surface to core, see for example, Renton (1999). Consider a square plate of the three lattices, comprising 100 cells × 100 cells, subjected to tensile loading and to shear loading. We shall show that both types of loading give rise to a deep boundary layer in the Kagome lattice but not in the two honeycombs. The Kagome lattice deforms by bar stretching in the bulk, while at the lateral surface of the reticulated plate, the connectivity is sufficiently low for bar bending to dominate the response. A finite transition zone is needed in order to switch the loading state from one to the other. In contrast, the hexagonal honeycomb deforms by bar bending at the surface and core, while the triangular honeycomb deforms by bar stretching both at the surface and core. Consequently, the St. Venant diffusion length is small for the honeycombs, on the order of one cell dimension.

7.1. Case a, normal loading

The sides are traction free, while the joints along the top and bottom faces are subjected to a displacement of $\bar{u}$ and $-\bar{u}$, respectively, along the x_2 direction. Additionally, along the top and bottom faces no constraint is imposed on the joints displacement in the x_1 direction (except for restraining one joint against rigid body motion in the x_1 direction) and free rotation is allowed. The elastic deformation response of each lattice has been calculated using the finite element procedure as detailed above for $\bar{\rho}$ in the range 0.01–0.2. Examination of the deformed mesh reveals that a deep boundary layer exists at the lateral sides of the Kagome lattice, see Fig. 11a. No such boundary layer is evident for the hexagonal and triangular lattices, and so images of the deformed mesh are not included: although the loading for the surface layer of cells is different from that of the core, the St. Venant distance for load diffusion is only about one cell dimension for both honeycombs.

The stress concentration factor associated with the presence of the free surface has been calculated for each lattice: the maximum value of local tensile stress within any bar of the surface cells σ_S has been calculated. In addition, the maximum local tensile stress σ_R in any bar of the cells within the bulk of the lattice (remote from the surface) has been calculated. The stress concentration associated with any surface boundary layer is given by the ratio $k_T \equiv \sigma_S/\sigma_R$, and this gives the predicted knock-down in tensile strength due to the presence of a free surface. It is found that the stress concentration factor k_T equals unity for the hexagonal and triangular honeycombs: no stress concentration exists for the hexagonal and triangular lattices. In contrast, for the Kagome lattice k_T drops from a value of 3.0 at $\bar{\rho} = 0.01$ to a value of 2.2 at $\bar{\rho} = 0.2$, see Fig. 12. The location of maximum stress is shown in Fig. 1(c) for the Kagome lattice: the location A marks a site of maximum tensile stress in

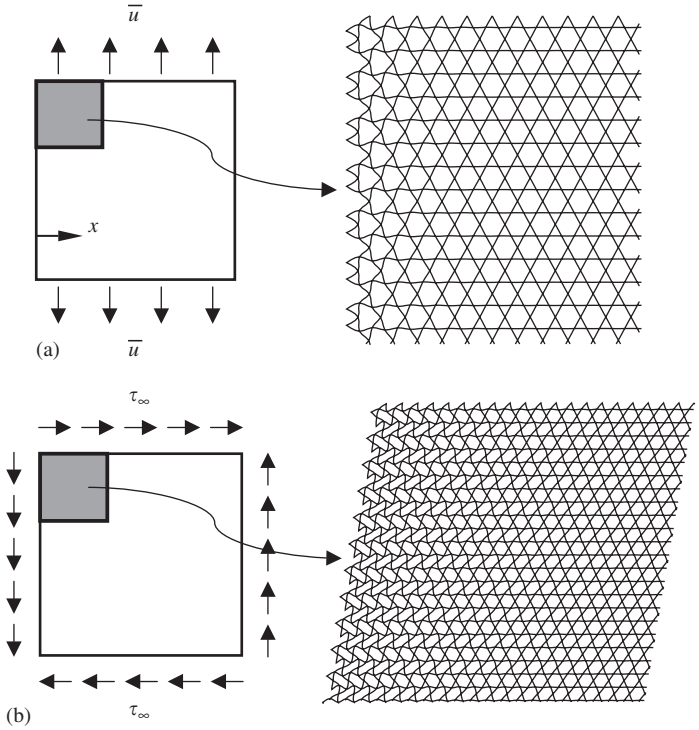

Fig. 11. Deformed mesh for Kagome lattice ($\bar{\rho} = 10\%$) revealing a boundary layer at the sides of the specimen for (a) uniaxial tension and (b) simple shear.

the surface cell, while the site B refers to a site of maximum local stress within the bulk of the Kagome lattice.

The sensitivity of the stress concentration factor in the Kagome lattice to lattice rotation was explored in a preliminary manner: finite element calculations were performed on the lattice loaded transversely rather than vertically. This corresponds to a lattice rotation of 30°. No boundary layer effect is observed for the rotated lattice: the stress state in the surface layers is identical to that sub-surface.

It is instructive to plot the traction distribution along the top of the Kagome plate for selected values of relative density, see Fig. 13. Upon writing x as the distance along the top of the plate from the top-left corner (along the x_1 direction), we find that the traction T in the x_2 direction scales with $\bar{\rho}x/\ell$, and is adequately fitted by the formula

$$T = T_0(1 - \exp(-4\bar{\rho}x/\ell)), \tag{32}$$

where T_0 is the traction at the centre of the plate. The exponential variation in traction is anticipated by an eigenvalue analysis using the transfer matrix method, or by Bloch wave theory: the detailed analysis of the boundary layer effect will be presented in a subsequent publication.

It is instructive to compare the boundary layer depth at the free surface of a Kagome plate (Fig. 13) with the length of elastic shear zones at a crack tip (Fig. 8). The boundary

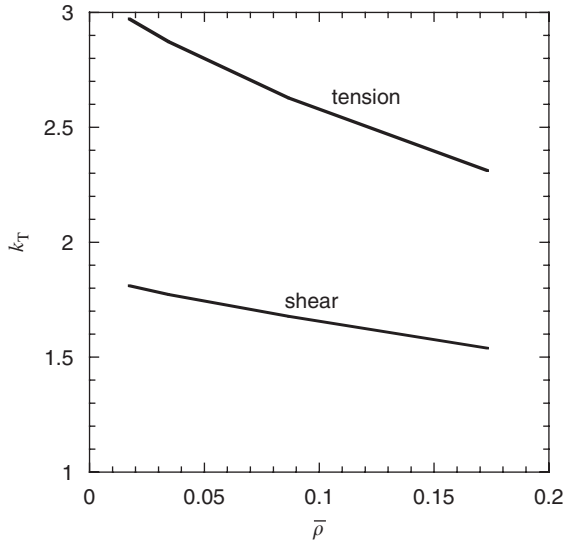

Fig. 12. Stress concentration factor at the edge of the Kagome lattice as a function of relative density.

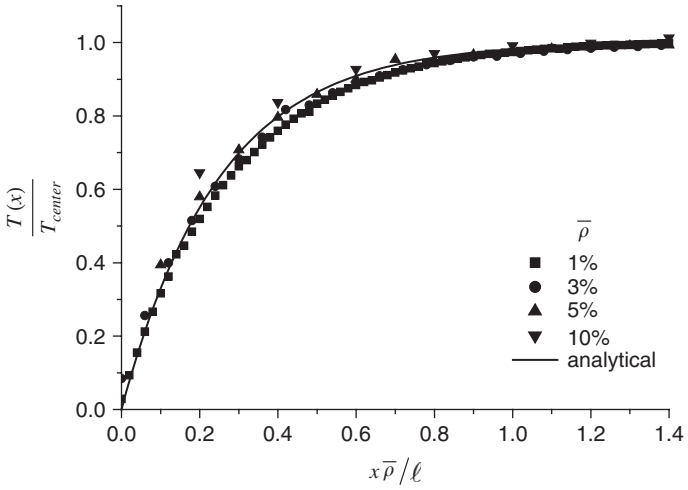

Fig. 13. Traction distribution along the top of the Kagome lattice, under tensile loading.

layer depth is of order $\ell/\bar{\rho}$ while the elastic shear zone ahead of a mode I or mode II crack is of order $4.5\ell/\bar{\rho}$. The decay length for an actuated Kagome structure is also approximately $4\ell/\bar{\rho}$, see Wicks and Guest (2004).

The boundary layer along the sides of the Kagome lattice provides insight into a paradox in the literature on the effective modulus of triaxial composites. Kueh et al. (2005) have measured the modulus and strength of carbon-fibre, epoxy-matrix composites with a Kagome weave and find that the elastic modulus is neither isotropic nor independent of the width of the specimen. Narrow specimens loaded in the direction shown in Fig. 11a have a lower modulus than wide specimens; and no such width effect is observed for specimens

loaded in the transverse direction. These observations are readily explained in terms of the compliant boundary layer of Fig. 11a.

7.2. Case b, shear loading

Finite element simulations have also been performed by applying uniform shear traction to each of the lattices in order to determine whether a boundary layer exists for shear loading. The deformed mesh is shown in Fig. 11b for the Kagome grid at $\bar{\rho} = 10\%$. Again, a boundary layer is evident along the sides of the lattice, and again this is due to the fact that the equilibrium state internal to the lattice cannot be sustained at the lateral surface. The depth of boundary layer in shear is comparable to that in tension, but the stress concentration associated with the boundary layer is somewhat less, see Fig. 12. The hexagonal and triangular honeycombs were also subjected to shear loading for $\bar{\rho}$ in the range $\bar{\rho} = 0.1-10\%$. No such boundary layers were observed.

8. Concluding remarks

This study has revealed a number of remarkable features of the Kagome lattice. It has an unusually high fracture toughness due to the presence of an elastic zone of bending emanating from the crack tip into a remote stretching field. The predicted fracture toughness scales as $\bar{\rho}^{1/2}$. In contrast, the triangular lattice stretches under all loading states and K_{1C} scales with $\bar{\rho}$. And the hexagonal honeycomb deforms by cell wall bending, such that K_{1C} scales with $\bar{\rho}^2$. The Kagome lattice exhibits pronounced crack tip blunting due to the deformation band at the crack tip; this blunting reduces the stress levels at the crack tip and thereby increases the fracture toughness.

The high fracture toughness of the Kagome lattice endows it with a high damage tolerance–at a low value of $\bar{\rho}$, the tensile strength of a centre-cracked panel made from the Kagome lattice is almost independent of crack length up to relatively large crack lengths. LEFM predictions are accurate for a semi-crack length exceeding a transition value of about $\ell/\bar{\rho}$. In contrast, the fracture strength of the centre-cracked panel made from the hexagonal and triangular lattice are sensitive to crack length, with LEFM predictions being acceptable for cracks longer than about one cell dimension.

This study has been limited to the elastic–brittle response of perfect lattices. In reality, lattices contain imperfections in the form of wavy and missing bars, and displaced joints. The effect of imperfection upon the fracture properties of the three lattices remains a topic for further study.

References

Brown, W.F., Srawley, J.E., 1966. Plane strain crack toughness testing of high strength metallic materials. ASTM STP410.

Chen, J.Y., Huang, Y., Ortiz, M., 1998. Fracture analysis of cellular materials: a strain gradient model. J. Mech. Phys. Solids 46 (5), 789–828.

Deshpande, V.S., Ashby, M.F., Fleck, N.A., 2001a. Foam topology: bending versus stretching dominated architectures. Acta Mater. 49, 1035–1040.

Deshpande, V.S., Fleck, N.A., Ashby, M.F., 2001b. Effective properties of the octet-truss lattice material. J. Mech. Phys. Solids 49 (8), 1747–1769.

dos Santos e Lucato, S.L., Wang, J., Maxwell, P., McMeeking, R.M., Evans, A.G., 2004. Design and demonstration of a high authority shape morphing structure. Int. J. Solids Struct. 41, 3521–3543.

Evans, A.G., Hutchinson, J.W., Fleck, N.A., Ashby, M.F., Wadley, H.N.G., 2000. The topological design of multifunctional cellular metals. Progr. Mater. Sci. 46 (3&4), 309–327.

Fleck, N.A., 1986. Finite element analysis of plasticity-induced crack closure under plane strain conditions. Eng. Fracture Mech. 25 (4), 441–449.

Fleck, N.A., Kang, K.J., Ashby, M.F., 1994. Overview no. 112: the cyclic properties of engineering materials. Acta Metall. Mater. 42 (2), 365–381.

Gibson, L.J., Ashby, M.F., 1997. Cellular Solids; Structure and Properties, second ed. CUP.

Huang, J.S., Gibson, L.J., 1991. Fracture toughness of brittle honeycombs. Acta Metall. Mater. 39 (7), 1617–1626.

Hunt, H.E.M., 1993. The mechanical strength of ceramic honeycomb monoliths. Trans. I Chem. E 71A, 257–266.

Hutchinson, R.G., Wicks, N., Evans, A.G., Fleck, N.A., Hutchinson, J.W., 2003. Kagome plate structures for actuation. Int. J. Solids Struct. 40, 6969–6980.

Kanninen, M.F., Poplar, C.H., 1985. Advanced Fracture Mechanics. OUP, Oxford, UK.

Kueh, A., Soykasap, O., Pellegrino, S., 2005. Thermo-mechanical behaviour of single-ply triaxial weave carbon fibre reinforced plastic. In: European Conference on Spacecraft Structures, Materials and Testing 2005, 9–13 May 2005, Noordwijk, The Netherlands.

Larsson, S.G., Carlsson, A.J., 1973. Influence of non-singular stress terms and specimen geometry on small-scale yielding at crack tip in elastic–plastic materials. J. Mech. Phys. Solids 21, 263–277.

Maiti, S.K., Ashby, M.F., Gibson, L.J., 1984. Fracture toughness of brittle cellular solids. Scripta Metall. 18, 213–217.

Renton, J.D., 1999. Elastic Beams and Frames. Camford Books, Oxford, UK.

Rice, J.R., 1974. Limitations to the small scale yielding approximation for crack-tip plasticity. J. Mech. Phys. Solids 22, 17–26.

Shercliff, H.R., Fleck, N.A., 1990. Effect of specimen geometry on fatigue crack growth in plane strain: II. Overload response. Fatigue Fracture Eng. Mater. Struct. 13 (3), 287–296.

Symons, D.D., Hutchinson, R.G., Fleck, N.A., 2005. Actuation of the Kagome double layer grid. Part 1: prediction of the performance of the perfect structure. J. Mech. Phys. Solids 53, 1855–1874.

Wadley, H.N.G., Fleck, N.A., Evans, A.G., 2003. Fabrication and structural performance of periodic metal sandwich structures. Compos. Sci. Technol. 63, 2331–2343.

Wicks, N., Guest, S.D., 2004. Single member actuation in large repetitive truss structures. Int. J. Solids Struct. 41, 965–978.

Williams, M.L., 1957. On the stress distribution at the base of a stationary crack. J. Appl. Mech. 24, 109–114.